Flooding Extent Mapping for Synthetic Aperture Radar Time Series Using River Gauge Observations

Tomasz Berezowski, *Member, IEEE*, Tomasz Bieliński, and Jakub Osowicki

***Abstract*—The flooding extent area in a river valley is related to river gauge observations such as discharge and water elevations. The higher the water elevations, or discharge, the larger the flooding area. Flooding extent maps are often derived from synthetic aperture radar (SAR) images using thresholding methods. The thresholding methods vary in complexity and number of required parameters. We proposed a simple thresholding method that takes advantage of the correlation between the river gauge and the flooding area. To show the applicability of the method, we used a 2014–2018 time series of 161 Sentinel 1 SAR images acquired over a wetland floodplain located in Northeast Poland. We validated the method by extracting local water line elevations from a high-resolution digital elevation model for three river gauges, which resulted in a root-mean-square error of 0.16 m, a bias of 0.07 m, and a correlation of 0.86 for the best scenario. The scenario analysis showed that the most important factor affecting the method's accuracy was a proper delineation of the zone in which the flooding extent area was calculated. This was because other water sources, uncorrelated with river flow, were present in the floodplain as open water. Additionally, higher accuracy was obtained for the VV than VH polarization. The discharge can be used instead of water elevations as a river gauge variable, but this results in more bias in the water extent estimates.**

***Index Terms*—Synthetic aperture radar, hydrology, rivers, floods, image classification.**

I. Introduction

FLOODING extent maps developed using satellite synthetic aperture radar (SAR) data have been providing valuable information for crisis response, ecology, or hydraulic modeling. So far, many methods have been developed, of which the most popular choose the radar backscatter threshold below which a SAR data pixel is labeled as flooded either in an automated way [1], [2] or by expert judgment [3]. These simple robust methods have limited applicability in difficult case studies, such as with complex topography or abundant vegetation, and therefore were modified or adapted in more complex methods [4], [5]. Recent examples of complex flood mapping methods used ancillary data and region growing [6], local correction algorithms of radar layover, and emergent vegetation [7], elevation-based filtering and processing in local tiles [8], or classification, including multistep classification, often followed by data transformation [9]–[12]. The disadvantages of complex methods are limited repeatability due to a lack of ready-to-use software and the need to provide parameter values (for some of the methods).

Long-term SAR sensor missions, such as PALSAR, Radarsat, and Sentinel 1, provide an opportunity to produce flooding map time series, which have been utilized in studies focusing on flood monitoring and ecology [13]–[18]. The time series has also been very useful for hydrodynamic model calibration and validation [9], [19], [20]. A deeper analysis of the time-series approach revealed that high spatial resolution of SAR data is more important than its temporal resolution in model calibration [21]. Moreover, the uncertainty of roughness parameters (one of the most important parameters of hydrodynamic models) is lower when the model is calibrated with SAR images taken before rather than during or after the flood peak [22]. These findings highlight the benefits of using high-spatial- and temporal-resolution flooding extent maps, which nowadays can be elaborated using contemporary SAR sensors.

Yet, as discussed before, more complex methods, which were often used for the elaboration of SAR flooding extent time series, are more difficult to use than simple robust methods. In contrast, simple methods lack features for automatic processing SAR data time series, which may lead to inconsistencies between the flood extents derived from subsequent images. To overcome this issue, a method that relates time series of SAR data with another observed variable, related to flooding extent, can be used. Flooding extent maps were used to derive time series of river discharge estimates in several British Columbia (Canada) [23] and South Korea [18] rivers. Another approach was to relate water depth in the Congo River (Africa) with SAR backscatter using satellite altimeter data instead of river gauge for observation [24]. Flooding extent maps were also used to derive a relation between water elevation and river extent for dike location prediction in two United Kingdom rivers [25].

These kinds of relations can be used conversely—to derive flooding extents using observed water elevations or discharges. In a preliminary study, this approach was used to estimate the backscatter threshold for flood mapping using a series of 120 SAR images and discharge observation in the Biebrza River wetland floodplain (Poland) [26]. That study used a search technique (similar to [18] and [25]) to find the optimal threshold by maximizing the correlation between flooding area and discharge. Effectively, the optimal correlation coefficient was 0.59, and a reasonable flooding extent was provided when compared to color-infrared satellite images. However, that study also indicated the limitation of this technique during wet conditions in

Manuscript received March 11, 2020; revised May 3, 2020; accepted May 17, 2020. Date of publication May 28, 2020; date of current version June 11, 2020. This work was supported by the National Science Centre, Poland, under Grant 2017/26/D/ST10/00665. *(Corresponding author: Tomasz Berezowski.)*

The authors are with the Faculty of Electronics, Telecommunication and Informatics, Gdańsk University of Technology, 80-233 Gdańsk, Poland (e-mail: tomberez@eti.pg.edu.pl; tomasz.bielinski@pg.edu.pl; osojak@gmail.com).

Digital Object Identifier 10.1109/JSTARS.2020.2995888

the floodplain (i.e., when water from other sources than the river is present) and the requirement of deeper validation.

In this study, we aim to perform further tests of an automated method for the radar backscatter threshold estimation using SAR imagery and observed hydraulic variables. We seek to investigate the effects of the polarization used (VV or VH), the extent of the zone used for calculation of the flooding extent area, and the observed hydraulic variable used, i.e., discharge or water elevations. We also perform validation of the estimated flooding extents by extracting the water line elevation in the neighborhood of three gauging stations. Finally, we discuss the method in the scope of providing data for integrated hydrological model validation.

II. Methods

A. Test Site and Data

The test site was located in the lower basin of the Biebrza River in northeastern Poland (see Fig. 1). The lower Biebrza basin is extensively flooded each year during spring and, therefore, provides a valuable record for analyzing flooding phenomena. The lower basin comprises 210 km^2 of which 12.5–141.2 km^2 were yearly flooded by river water in the 1966–2000 period [27]. Apart from the river water flooding, the lower basin is inundated by water from groundwater discharge and local rainfall and snowmelt. The extent of water from each source and its proportion is time variant during the flooding. However, in general, the river water is clustered along the Biebrza River and its tributaries, groundwater is discharged at the basin margins, and the rainfall and snowmelt are dominant elsewhere [28]–[30]. The lower basin wetland is a NATURA2000 and a Ramsar site; it has National Park status in Poland and is a reference area for wetland research [31]. Vegetation is dominated by various wetland communities, which include mostly meadows, sedges, reeds, bushes, and their mosaics [32]. Human impact is low, limited only to mowing and forestry, a sparse network of unpaved roads and ditches, and several settlements located on dunes or the basin margin. The Biebrza River catchment is of medium size, comprising 7000 km^2, and the lower basin is located just above the confluence of the Biebrza and Narew Rivers. Therein, the daily discharge (1951–2017) ranged between 4.33 and 517 m^3/s with an average of 34.7 m^3/s. During the 2014–2018 study period, the discharge ranged between 5.18 and 135 m^3/s, which corresponds to the water elevation range between 99.79 and 102.42 m above mean sea level (AMSL) (the Kronsztad 86 elevation reference system was used in this study as the mean sea level).

1) Hydrological Data: We used the discharge and water elevation daily data from three cross sections: the upstream cross section (Osowiec), the cross section located on a tributary in an upper part of the basin (Rudzki), and the downstream cross section (Burzyn) (see Fig. 1 and Table I). The water elevations were directly measured at the gauge, whereas the discharges were obtained based on a water depth–discharge relation, usually as a power-law function. The relation between water depth and discharge is often equivocal; therefore, for one gauge, a few power-law functions can be established. Moreover, the discharge is usually further corrected according to readings at the subsequent river gauges to maintain the water balance. These preprocessing steps were conducted by the Polish Institute of Meteorology and Water Management—National Research Institute (PIMWM), which manages the gauges and provided the data [33]. We recalculated the water elevations from the Kronsztad 60 to Kronsztad 86 elevation reference system by

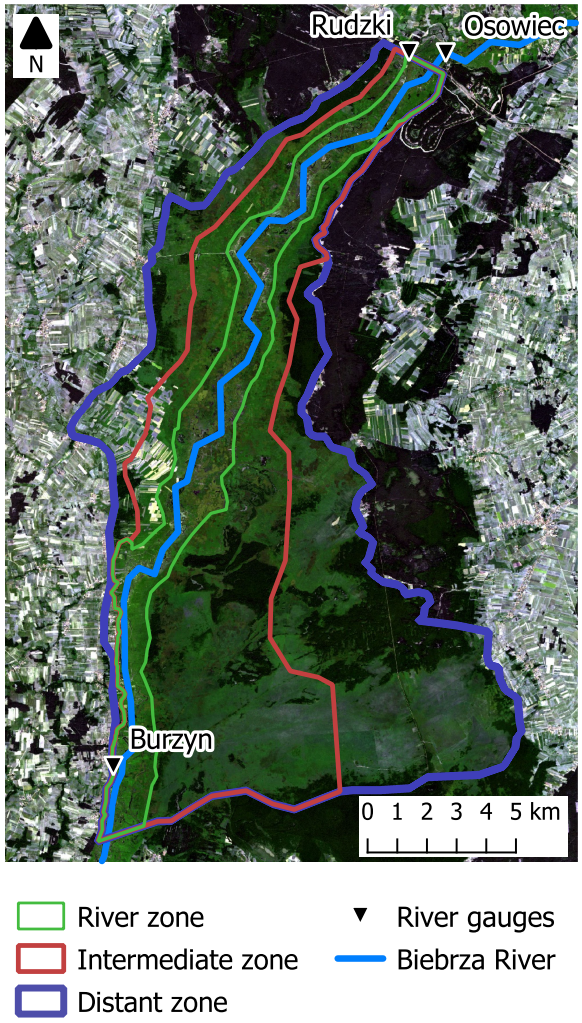

Fig. 1. Study area with the Biebrza River (blue line, flow direction north to south), river gauges (black triangles), and zones for flooding area calculation (color polygons). The lower basin extent is the same as the extent of the distant zone. The background image is the Sentinel 2 true color composition acquired on June 9, 2018, where dark green patches are forest, bright green patches are nonforest wetlands, and gray and bright green mosaics are agricultural areas.

TABLE I
Characteristics of Three River Cross Sections Used in the Study

Cross-section	River width [m]	Approximate fluvial terrace width [m]	Average discharge [m^3/s]	Water elevation ranges [m]
Burzyn	29	1500	34.7	2.99
Osowiec	21	1860	22.3	2.66
Rudzki	13	490	9.6	1.59

River widths were averaged from several cross sections around the river gauge. The fluvial terrace width includes manmade embankments in the neighborhood of the Osowiec and Rudzki cross sections. Average discharge and water elevation ranges (maximum and minimum water elevation difference) 1951–2017 were provided by PIMWM [33].

subtracting 0.125 m from the original elevation in Burzyn and Osowiec and 0.08 m for Rudzki.

2) Elevation Model: The digital terrain model (DTM) used in this study was elaborated based on an aerial laser scanning campaign conducted in December 2015 and was provided by the Biebrza National Park in the Kronsztad 86 reference system in a 0.50-m grid [34]. The laser scanning was conducted after the growing season, which allowed for good estimation of the terrain elevation, which was crucial for the analysis of the flooding extent. The DTM model had all surface objects removed, leaving only the "bare earth" elevation.

3) Snow Data: The Biebrza catchment is located in the coldest region of the lowlands of Poland with long persisting snow cover [35]. Snow cover increases SAR backscatter in comparison to bare earth backscatter [36]. Therefore, we were interested in assessing the quality of the method during days without the presence of snow cover. Daily snow cover for the lower basin was obtained from the IMS 4-km Snow Cover Data product [37]. We also used PIMWM snow depth data [33] from two stations (Rożanystok and Pieńczykówek), which surround the lower basin, to enhance snow detection during low snow depths. We were interested only in the presence or absence of snow. Hence, we blended both snow products using the following rule: if snow was present in any of the snow products, then snow was present in the study area. During the 2014–2018 period, snow cover was present for 19% of the time in the blended product and for 15% of the time in the IMS snow product.

4) SAR Data and Processing: We used Sentinel 1 A/B ground range detected (GRD) images downloaded from the Copernicus Open Access Hub and Alaska Satellite Facility servers. Images were downloaded for the entire Sentinel 1 availability period at the beginning of the research, i.e., from October 18, 2014 to November 18, 2018. Any image that at least partially intersected the study area was selected; however, from all available images, we used only relative orbit 153. In total, 218 images were downloaded, from which 106 covered the study area partially and required mosaicking. As a result, SAR images from 161 days in the 2014–2018 period were available after mosaicking.

We processed the Sentinel 1 images automatically using the snappy package, which is a python extension of the ESA SNAP 7.0 software. The processing consisted of several steps applied in the following order: application of the precision orbit file, radiometric calibration to backscatter coefficient (σ^0) [dB], mosaicking images partially covering the study area from two available images for a given day, cropping the images to the bounding box of the study area, speckle filtering using the Lee filter in a 3×3 pixel kernel, and finally range-Doppler terrain correction with projection to the local PUWG 1992 (EPSG:2180) coordinate system. After the processing, each image size was 4936×6905 pixels, with a pixel rectangular size of 6.4 m.

B. σ^0 Threshold Estimation Method

The method finds a threshold value (t_0) [dB] of σ^0 for optimal discrimination between flooded and nonflooded pixels. The main assumption was that the water elevation (h) [m AMSL] at a river valley cross section is correlated with the flooded area (u) [m^2] in a certain zone around the cross section. The river valley zone in which the flooded area was calculated had to be delineated beforehand, as described in the further paragraphs of this section and in Section II-C. The relation depends on the water flow and the relief of the river valley, but in a river valley with an ideal trapezoidal cross section and water slope equal to the valley slope $u \propto h$. Using this relationship and the standard thresholding technique for flooding extent mapping, the t_0 threshold was estimated by finding the maximum correlation between SAR-derived flooding areas $U(t) = (u_1(t), u_2(t), \ldots, u_n(t))$ and an n-day series of water elevations measured at the river gauge $H = (h_1, h_2, \ldots, h_n)$:

$$t_0 = \underset{t \in [-30,-14]}{\arg\max}\ f(t) \tag{1}$$

where

$$f(t) = \operatorname{cor}\left(U(t), H\right) \tag{2}$$

and the flooded area for a single SAR image $u_i(t)$ [m^2] was calculated as a sum of flooded raster cells in a river valley zone:

$$u_i(t) = \sum_{j=1}^{m} \begin{cases} c, & \sigma_{ij}^0 \le t \\ 0, & \sigma_{ij}^0 > t \end{cases} \tag{3}$$

where σ_{ij}^0 was the backscatter coefficient for the SAR image i and raster cell j, m was the total number of raster cells in a river valley zone, and c was a raster cell area [m^2]. Because (1) was a 1-D problem, we looked for arg max (argument of the maxima) by screening the -30 to -14 dB domain rather than using a nonlinear solver. The relation between u and h was unknown, however, and since we expected a relation that would be close to linear, we used Pearson's correlation in (2). To summarize, the method consists of the following steps.

1) A t value is assigned by the screening algorithm.
2) All SAR images are subjected to thresholding using t.
3) Flooded area $u_i(t)$ is calculated in the river valley zone for each SAR image i from 1 to n.
4) Correlation between $U(t)$ and H is calculated, and the result is paired with the current t.
5) Steps 1–4 are repeated for all t values in the screening range.
6) t_0 is equal to t with the highest correlation value.

Similarly to the u–h relationship, discharge (q) [m^3/s] at the cross section can be related to the upstream flooded area, because the discharge is nonlinearly related to the water depth. In such a case, in (2), $Q = (q_1, q_2, \ldots, q_n)$ would be used instead of the H series.

The river valley zone around the river gauge [i.e., the extent of m raster cells in (3)], which is further referred to as "zone," can be delineated in different ways. The zone can be characterized by the length along the river and the width perpendicular to the river. Each dimension cannot be very small, because a low m will produce a nonrepresentative pixel set for the u_i calculation. The zones have to be carefully selected by taking into account the river valley hydrology (e.g., the presence of large tributaries)

and geomorphology (e.g., fluvial terraces). Alternatively, semi-automatic methods such as HAND [38] can be used.

SAR sensors have different polarimetric capabilities, which allow the use of σ^0 for various polarizations (i.e., HH, VV, HV, or VH) in (3). The σ^0 decrease due to the specular reflection of the radar beam from the water is observed in each polarization; however, the HH polarization is considered best for flooded and nonflooded pixel discrimination in the C-band [12], [39].

C. Scenarios

We set up 12 experimental scenarios to examine the effect of river gauge variables, zones for flooding area calculations, and SAR data polarizations on the estimation of the t_0 threshold.

Two river gauge variables were used: water elevation and discharge at the Burzyn cross section. This differentiation allowed us to test whether the discharge, which is nonlinearly related to the water depth, would produce a different estimation of t_0 than the water elevations.

For each observation series, the effect of calculating the flooding area in one of three zones (river, intermediate, or distant; see Fig. 1) was examined. Each of the zones had the same length of approximately 40 km along the river, starting downstream of the Burzyn cross section and ending near the Osowiec cross section. However, the zones had different widths, which allowed looking at the effect of flooding from different water sources. The river zone was delineated only in the fluvial terrace, where the oxbow lakes are present and which has the lowest elevation in the basin. This zone was the most frequently flooded by the river water. The distant zone covered the entire lower basin with the boundary at the basin's margin. In this zone, all water sources were present, including groundwater discharge, rain, and snowmelt. The intermediate zone border was delineated halfway between the river and distant zone borders using the Thiessen polygon method. Even in this zone, extensive river flooding was expected, but not as extensive as in the river zone, and the water from groundwater, rain, and snowmelt also produced flooding. Although the distinctive zonation for river and nonriver flooding is present in many river valleys [40], it is not present in all cases. Because of that, one should investigate the hydrological behavior of a study area before the zone delineation.

Furthermore, for each zone, the effect of the SAR data polarization used for thresholding was examined. Most Sentinel 1 data available in the archives are in its primary mode: interferometric wide swath in dual-polarization VV+VH. Therefore, two polarizations were examined in thresholding: VV and VH.

D. Validation

We validated the method using water elevation (z_i) [m AMSL] data from river gauges located at the following cross sections: Burzyn, Osowiec, and Rudzki (see Fig. 1). The flooding extent water elevations ($\hat{z}_i$) [m AMSL] near the gauges were obtained from the water lines. The water lines were extracted by intersecting the DTM with the flooding extents $U(t_0)$ in the patches of low vegetation. The low vegetation patches were delineated by comparison of the DTM with the digital surface model, which, contrary to the DTM, also included the elevation of vegetation and other objects. Furthermore, we delineated the patches such that the distribution of elevation ranged from the river's bank elevation up to an elevation exceeding the maximum elevation expected from z_i. The intersection of a flooding extent $u_i(t_0)$ with the DTM yielded a sample of flooded DTM pixels in the river gauge proximity. From this sample, the maximum elevation was used as $\hat{z}_i$. The quality of the flooding extent was quantified by

$$\mathrm{RMSE} = \sqrt{\frac{\sum_{i=1}^{n} \left(\hat{z}_i - z_i\right)^2}{n}} \tag{4}$$

and

$$\mathrm{RMSE}\% = \frac{\mathrm{RMSE}}{\max_{i=1}^{n} z_i - \min_{i=1}^{n} z_i} 100\%. \tag{5}$$

The RMSE [m] quantified the flooding extent elevation error as an absolute figure, whereas the RMSE% [%] quantified the RMSE as a percentage of the data range. The optimal value of both RMSE and RMSE% is zero, which indicates a perfect match of the variables. Additionally, the mean error [m], or the bias, was calculated to show whether the method overestimates (positive ME) or underestimates (negative ME) the flooding extent elevation

$$\mathrm{ME} = \frac{\sum_{i=1}^{n} \left(\hat{z}_i - z_i\right)}{n}. \tag{6}$$

Finally, Pearson's correlation coefficient (ρ) [$-$] between z_i and $\hat{z}_i$ was calculated to quantify their linear dependence.

This validation was suitable only for flooding conditions, i.e., when the water elevation was above the river's bankfull level. This was because the rivers in the Biebrza catchment are too narrow for water elevation estimation using the water line extraction method when the water is inside the river channel. Yet, we were interested in the flooding extents, not the extent of the water in the river; therefore, validation only for flooding conditions was appropriate.

Because of the presence of snow and surface water from sources other than the river, we conducted the validation only using a subset of water elevation observations. We excluded periods of snow cover presence and periods, in which the water elevations were below the bankfull level. This subsetting resulted in a validation set size of 54 days for Burzyn, 49 days for Osowiec, and 16 days for the Rudzki cross section, which accounted for 63%, 61%, and 55% of the flooding times, respectively.

III. Results

A. Threshold Estimation

The t_0 took values from the range -24.9 to -23.0 dB for the VH polarization, and -19.0 to -17.2 dB for the VV polarization (see Fig. 2). The t_0 values were always the highest for the river zone and the lowest for the distant zone when looking at groups defined by polarization and river gauge variables. The correlation corresponding to the t_0 values ranged between 0.52 (for the distant zone, the VH polarization, and the discharge as a river gauge variable) and 0.73 (for the river zone, the VH River

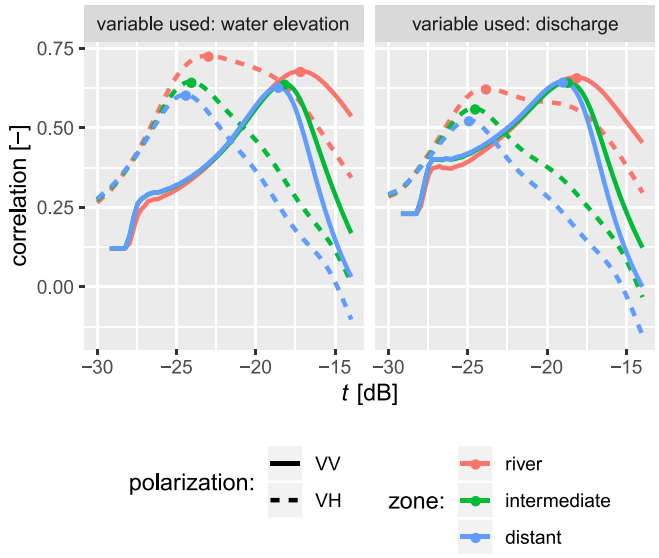

Fig. 2. Correlation, calculated using (2), between flooding areas $U(t)$ in a range of t values and water elevations (left panel) or when discharge (right panel) was used as an observation series. Except for the observation series used, the scenarios were varied by the zone used for the flooding area calculation (line colors) and polarization of the SAR images (dashed or solid lines), as described in Section II-C. The t_0 values for each scenario, calculated using (1), correspond to the peak of each line (dots).

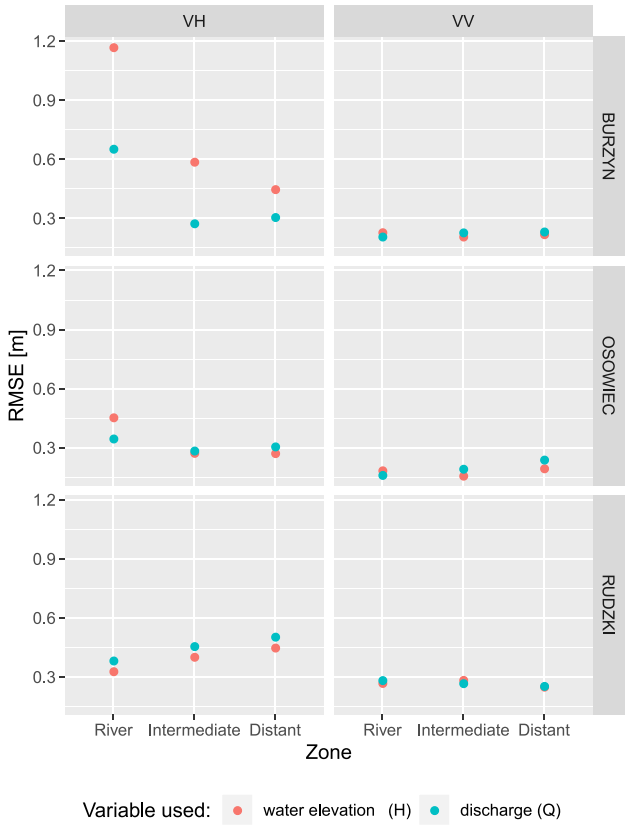

Fig. 3. RMSE for three validation cross sections (rows) in the study area. For each cross section, the RMSE for 12 testing scenarios is shown: three polarization combinations (columns), zones (x-axis), and observation series (point's color).

widths were averaged from several cross sections around the river gauge. The fluvial polarization, and the water elevation as a river gauge variable).

B. Validation

The RMSE ranged between 0.21 and 1.17 m for Burzyn (RMSE%: 25–139%), 0.16 and 0.46 m for Osowiec (RMSE%: 19–53%), and 0.25 and 0.51 m for Rudzki (RMSE%: 97–194%) (see Fig. 3). The lowest RMSE values were obtained for the VV polarization scenarios. The use of the VH polarization increased the RMSE by 0.21 m on average in comparison to VV scenarios. Overall, the errors in the water elevation scenarios were lower than those in the discharge scenarios: for 11 out of 18 cases, the RMSE for the water elevations was lower than that for the discharge. Yet in the river zone, in the VV polarization scenarios, the RMSE for the discharge was either lower than that for the water elevations or nearly the same (0.01-m difference in the Rudzki river gauge). The average RMSE difference between 18 water elevations and 18 discharge cases was lower than 0.01 m. No significant trend was found between the RMSE and the extent of the zones when grouping all cases.

The ME ranged between −0.18 and 0.50 m for Burzyn, −0.15 m and 0.21 m for Osowiec, and −0.32 and 0.05 m for Rudzki with negative bias for the 27 out of 36 cases (see Fig. 4). In each case, the nearest to zero bias was present for one of the water elevation scenarios. The average ME difference between 18 water elevations and 18 discharge cases was 0.10 m. Overall, the VV scenarios and the river zone scenarios were the least biased. In the river zone scenarios, the least bias was not present for two cases: VH in Burzyn and VH in Osowiec, where the intermediate zone scenarios were the least biased. The ME significantly decreased with the increasing zone extents when grouping all cases.

The correlation ranged between 0.12 and 0.76 m for Burzyn, 0.23 and 0.87 m for Osowiec, and 0.14 and 0.68 m for Rudzki with the overall strongest correlation in VV scenarios (see Fig. 5). The correlation was stronger for the water elevation than for the discharge for nine cases, and the opposite situation was also present for nine cases. The average correlation difference between water elevations and discharge scenarios was 0.05. No significant trend was found between the extent of the correlation and zones when grouping all cases.

Out of the tested scenarios, the best was with the VV polarization, water elevations, and the river zone used.

The temporal variation of error in the three tested cross sections for the best scenario shows that water elevations extracted from the estimated flooding extent matched well with the observed water elevations during the flooding period (see Fig. 6). The mismatch during the flooding period increased when snow cover was present. Missing values (false negatives) were present when the water elevation approached the bankfull level. Within all testing scenarios, the false negatives accounted for 4%. During the low flood periods, when the water elevation was below the bankfull level, false positives were present. They occurred in the majority at the beginning of the flooding period,

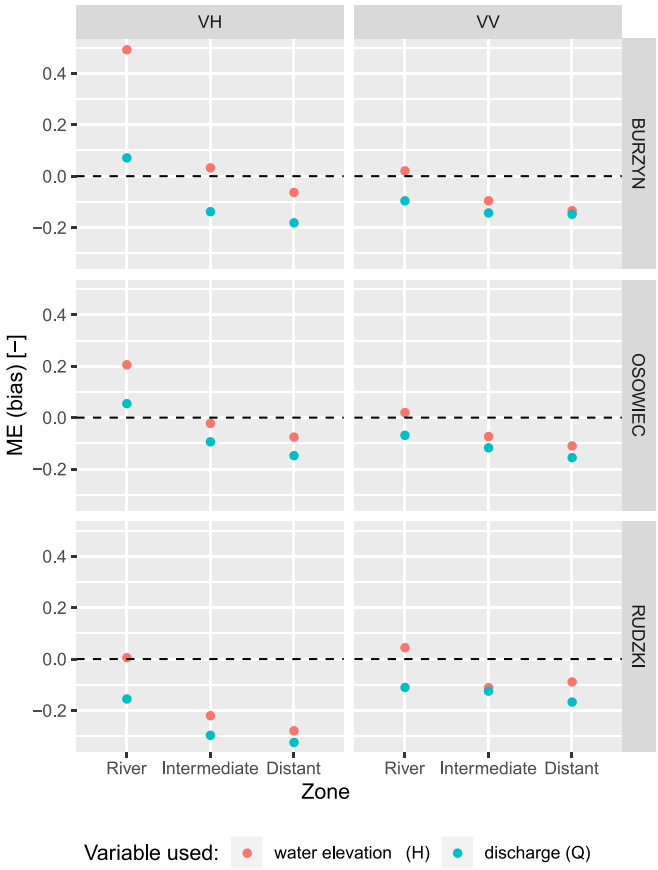

Fig. 4. ME, or bias, for three validation cross sections (rows) in the study area. For each cross section, the ME for 12 testing scenarios is shown: three polarization combinations (columns), zones (x-axis), and observation series (point's color). The dashed line in each panel indicates ME $= 0$ m, i.e., no bias.

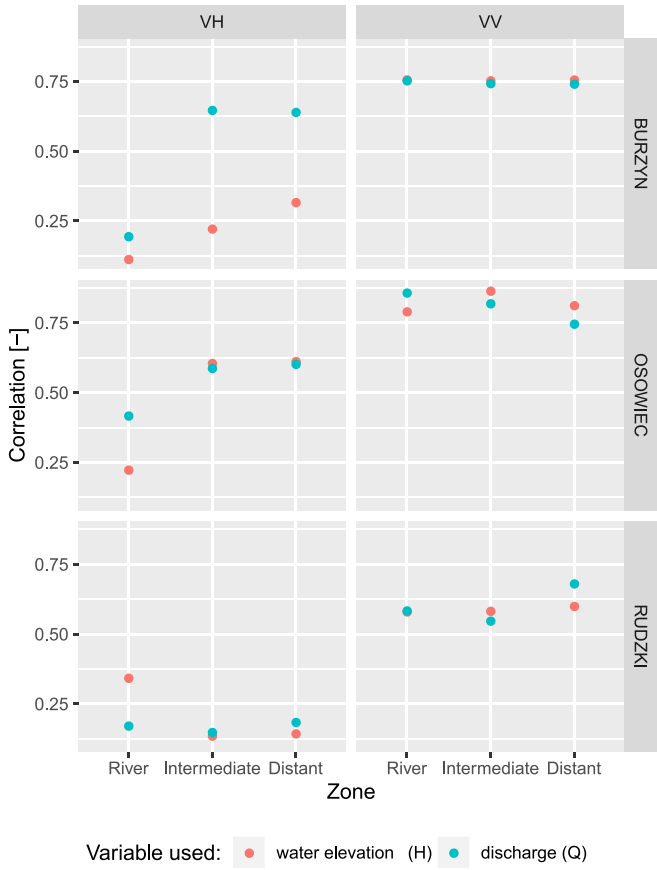

Fig. 5. Pearson's correlation coefficients (ρ) for three validation cross sections (rows) in the study area. For each cross section, ρ for 12 testing scenarios is shown: three polarization combinations (columns), zones (x-axis), and observation series (point's color).

but before the water elevation was above the bankfull level; they were also present during the snow periods. Notably, the false positive $\hat{z}_i$ had high values, which were often the highest values of all $\hat{z}_i$ and z_i. Within all testing scenarios, the false positives accounted for 13%.

C. Flood Mapping

Flooding extent was present mostly in the fluvial terrace, in an approximately 1–2-km buffer (see Fig. 7). However, flooding on remote parts of the floodplain was also observed. The presence of snow cover or wet conditions affected flood identification both in the fluvial terrace and in the remote parts of the floodplain (see Fig. 7). The effect of snow cover, although not always observed, was exhibited in two ways: either as underestimation of the expected flooding extent (e.g., January and February 2018 in Fig. 6 and snow presence/absence comparison in Fig. 7) or as overestimation of the expected flooding extent, which occurred mostly at the beginnings and ends of the snow periods (see Fig. 6). Underestimation of the expected flooding extent by the presence of snow cover was less evident for VH polarization than for the VV polarization data (see Fig. 7). The presence of wet conditions (i.e., high groundwater elevation and high soil moisture) always resulted in increased flooding extent in reference to the flooding extent expected from river flooding alone. This effect is illustrated by the false-positive estimation in Fig. 6 and the comparison of dry/wet conditions in Fig. 7.

The characteristics of flooding extent varied from more homogeneous in the VV polarization to more patchy in the VH polarization (see Fig. 8). The estimated flooding extents decreased when zones distanced further from the river were used. This effect was more evident for VH polarization than for VV polarization. The use of VH polarization resulted in erroneous identification of flooding in the agricultural areas (bare soil and young crops), which was not the case of VV polarization (western area in Fig. 8). The VH polarization also identified more flooding in a densely vegetated wetland area, which was unlikely to have been flooded by river water in the analyzed period (see Fig. 8). None of the analyzed scenarios was able to identify flooding below trees or dense vegetation cover.

IV. Discussion

A. Testing Scenarios and Validation

The estimated values of t_0 varied mostly with the polarization because water has higher copolarized scattering than volume

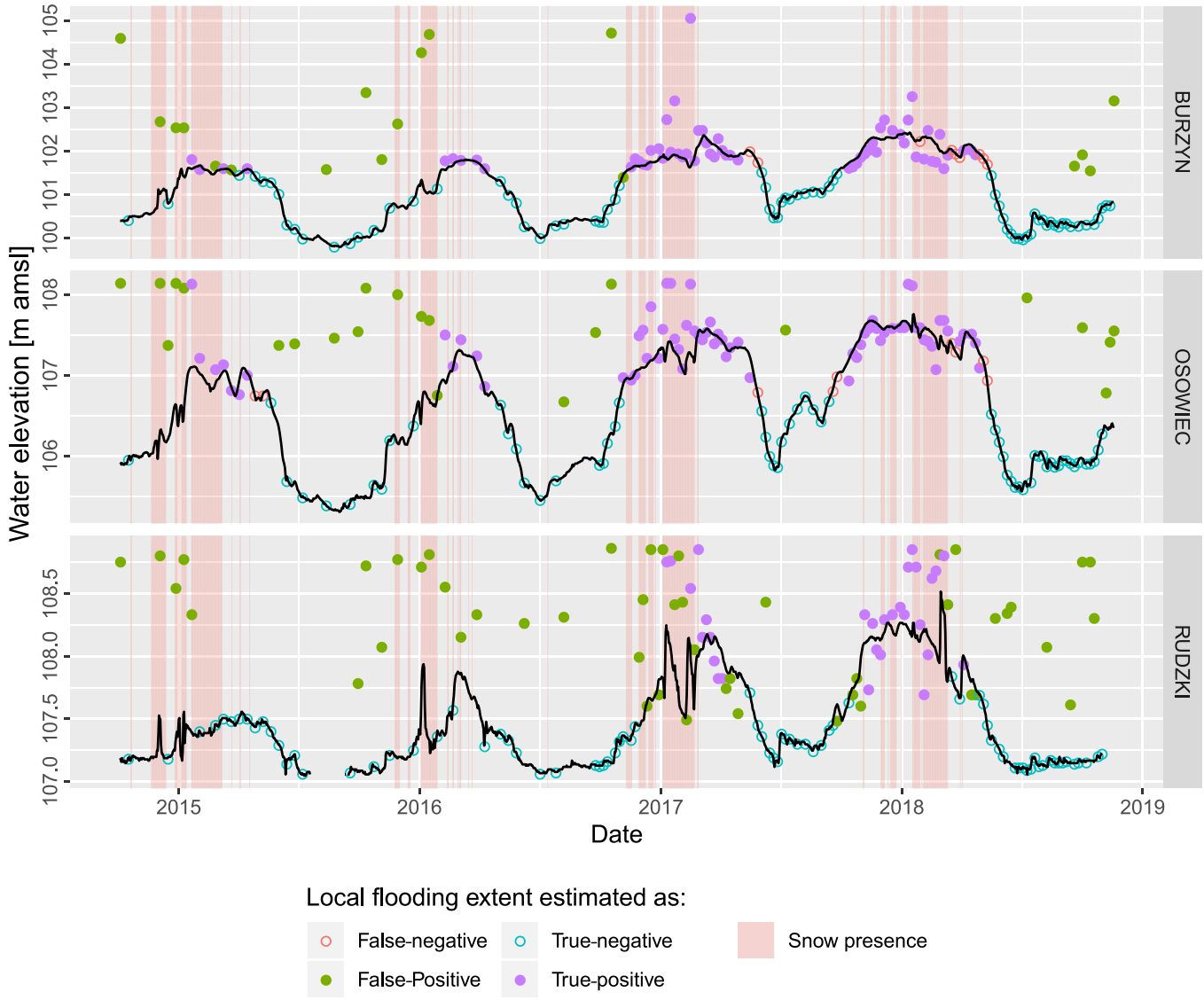

Fig. 6. Comparison of water elevations extracted from the estimated flooding extent ($\hat{z}_i$) and the observed water elevations (z_i) for the three tested cross sections for the VV polarization, water elevations used as an observed variable, and the river zone. True-positive estimation was done when z_i was above the bankfull level and $\hat{z}_i$ was not missing. False-positive estimation was done when z_i was below the bankfull level and $\hat{z}_i$ was not missing. True-negative estimation was done when z_i was below the bankfull level and $\hat{z}_i$ was missing. False-negative estimation was done when z_i was above the bankfull level and $\hat{z}_i$ was missing. Note that in the case of true-negative and false-negative cases, the empty dots show the day of Sentinel 1 acquisition, but the water elevation corresponds to z_i, not $\hat{z}_i$, because $\hat{z}_i$ was missing. Conversely, the filled dots indicate the day of Sentinel 1 acquisition and $\hat{z}_i$. Black lines indicate observed water elevations. Periods with snow cover are indicated by a reddish background.

scattering [41], [42]. The pattern of lower t_0 values for copolarized images confirms earlier observations of the Radarsat C-band sensor [39].

The VH scenarios were characterized by higher errors and lower correlations than the VV scenarios, which suggests that VH data are less suitable for flooding extent mapping than VV data using this method. Other studies agree with this; however, there are some exceptions. VH data have larger backscatter variability than VV data, which leads to potential misclassification with open water and enlargement of the flooding extents [8], [16], [43]. The radar data can also misclassify open water as bare soil due to the similar backscatter [44]; this was the case in our study for the VH polarization in the upland agricultural areas. False positives may also occur for flat man-made objects, such as roads, parking lots, and airfields [12]; this was not the case in our case because of the low degree of urbanization in the study area. In contrast, the inclusion of VH data into flood monitoring analyses can be beneficial in comparison to using VV data alone; the effect is, however, study site specific [10], [45]. Moreover, multi-data-source methods can benefit from C-band VH by exploring other properties of this polarization, such as its lower sensitivity to surface water roughness than VV data [12].

The second factor differentiating the t_0 values were the zones. Within the distant zone, and to a smaller extent within the intermediate zone, flooding occurs due to factors other than the river (i.e., groundwater discharge, rainfall, and snowmelt) [30].

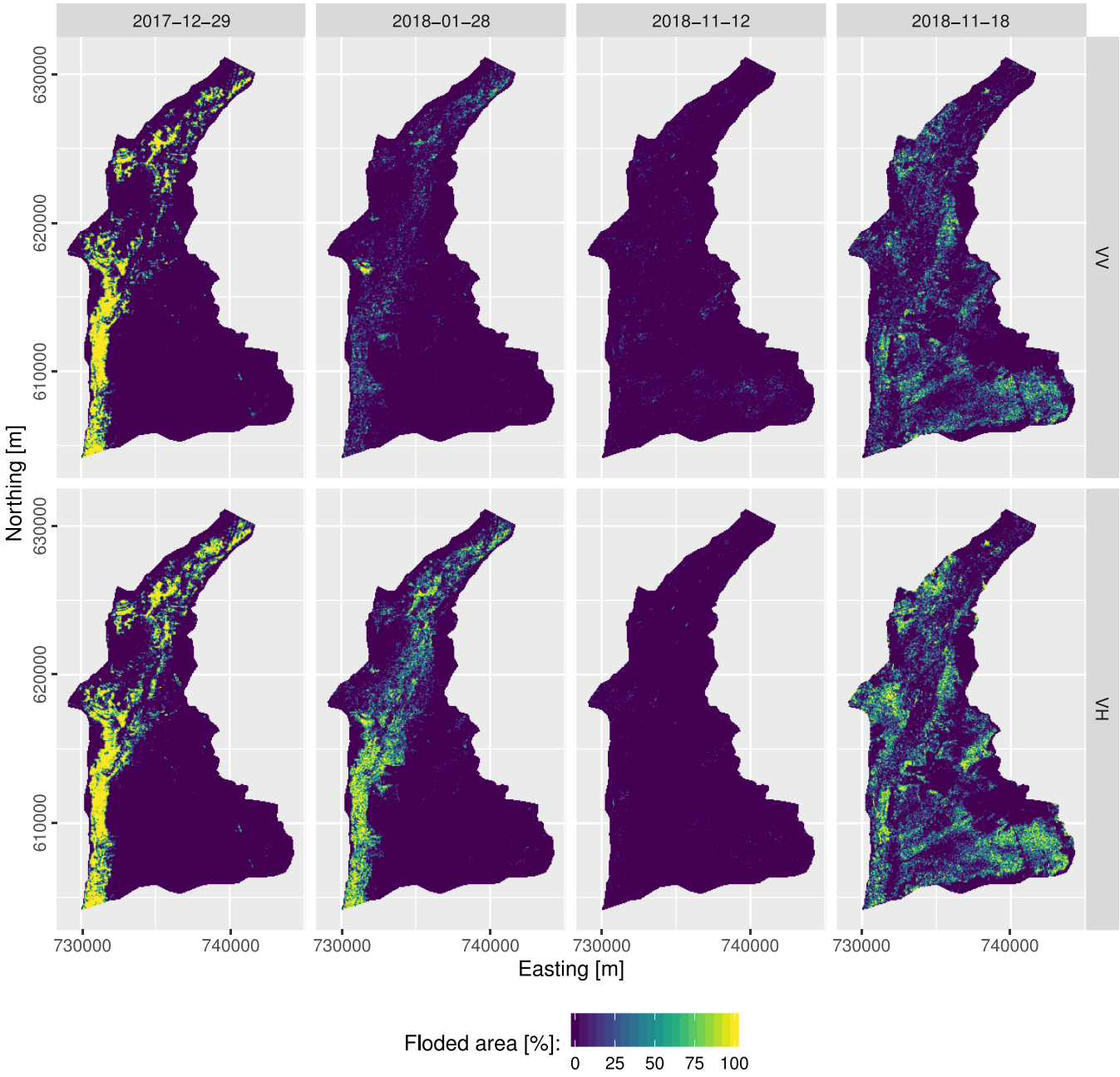

Fig. 7. Flooding extents estimated using the water elevations and the river zone in VV and VH polarizations (rows) for four time snapshots (columns). The first two snapshots compare snow absence (December 29, 2017) and snow presence (January 28, 2018) conditions during the same event and similar water elevations. The second two snapshots compare dry (November 12, 2018) and wet (November 18, 2018) conditions during the low flow period. The original pixel resolution of the flooding extents was aggregated tenfold for clarity of presentation; therefore, the color scale represents a per pixel flooding area percentage.

Flooding caused by these factors has different timing and is not as strongly correlated with the water elevation or discharge as river flooding. Therefore, maximization of the correlation between $U(t)$ and H or Q led to lower t_0 values for the distant and intermediate zones than for the river zone. Effectively, flooding extents estimated with the use of these zones were smaller than when the river zone was used. This effect was also reflected in the closer to zero ME values in the river zone in comparison to the two remaining zones.

Notably, other validation figures, RMSE and ρ, do not follow that ME dependence, especially in the VH scenarios. This is because the VH data produced a very patchy flooding extent with a considerable amount of false positives in the upland agricultural areas. This led to the underestimation of the flooding extent in the river valley with a high magnitude of RMSE and low ρ. Decreased t_0 values in VH polarization in the intermediate and distant zones (in comparison to the river zone) led to a decreased number of false positives in the agricultural area, which further

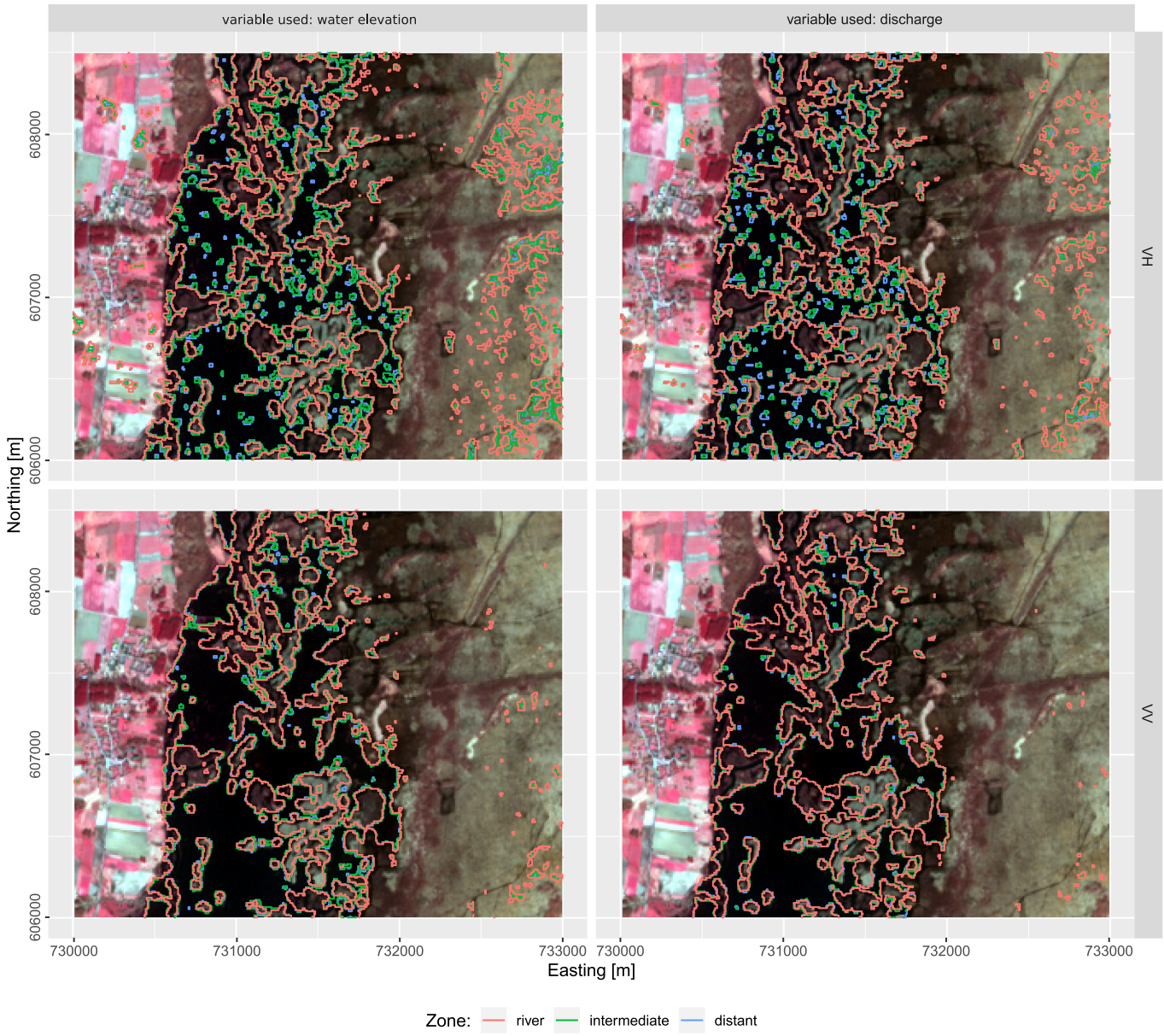

Fig. 8. Flooding extent boundaries extracts estimated on April 4, 2018 from the testing scenarios varied by zones (line colors), polarization (rows), and observation variables used (columns). The background image is an extract of a color infrared Sentinel 1 scene at 10-m spatial resolution acquired on April 10, 2018.

decreased the RMSE and increased ρ. The estimated flooding extent in the river valley was smaller; hence, the bias in the intermediate and distant zones was more negative than for the river zone.

These results indicate that the selection of the proper zone for the flooding area calculation [see (3)] is a key factor in the estimation of t_0 in our method. In another study, errors in the zone shape delineation led to errors of up to 13% in flooding extent estimation [23]. The zone delineation can be challenging especially when data on spatial river flooding frequency or fluvial terrace locations are missing. Selecting a too narrow (too close to a river) zone is better than selecting a too wide zone, which would also include considerable flooding from sources other than the river. We used a wide zone in a former study, which led to results comparable to those obtained by the distant zone in this study [26].

Other studies did not focus a lot on the shape of the zone, which was mostly due to looking at the river and its neighborhood rather than at the entire floodplain. If the extent of the water in the river is of interest, then the zone is delineated between the river banks only. This, however, required a 10–20 times wider river than in our study [18]. In that case, the zone selection is optimized not across the valley, as in our study, but along the river [18]. Alternatively, the zone can also be delineated for the local envelope of the river braids or meanders [3], [23]. A straightforward zone delineation is possible in regulated streams, where zones comprise the area between the dikes [25]. Another approach of zone delineation is to find a location that

is very responsive to water elevation changes, e.g., due to the presence of characteristic vegetation. Such local zones are used rather for water depth modeling than for flood mapping [24].

The use of the water elevation instead of the discharge as a river gauge variable resulted in the least bias in the water extent elevation estimates. This was most likely because of a nonlinear relation between the flooding extent area and the discharge, whereas the relation between the water elevation and flooding extent area can be closer to linear. This was expressed by the higher correlation between flooding extent areas and water elevations than discharges at t_0 (see Fig. 2). Yet, other validation criteria presented similar figures for both water gauge variables, which makes discharges a reasonable alternative to use in this method when water elevations are not available.

B. Flood Mapping

Overall, the flooding extents estimated by our method were accurate in Osowiec and Burzyn cross sections, whereas the errors were higher in the Rudzki cross section. This was because the channel and fluvial terrace width, as well as the discharge at the Rudzki cross section, were much smaller than in the two remaining cross sections, and the flood extent detection at the Sentinel 1 resolution was more challenging. Yet, our method was able to identify the flooding extent elevation with a 0.25-m RMSE at the Rudzki cross section.

In contrast, the flooding extents estimated by our method have several shortcomings:

1) patchy pattern caused by obscuring the water by emergent and riparian vegetation;
2) inability to distinguish between river water flooding and flooding caused by groundwater discharge, rain, or snowmelt;
3) misclassification due to snow cover;
4) false-negative estimates at the end of the flooding period.

A patchy pattern due to vegetation is often present in nonarid study areas. Several processing steps have been proposed to produce continuous flooding extents, e.g., region growing [7], [12], [17], [46], rule-based algorithms [6], multitemporal analysis [10], [14], [45], wavelet analysis [47], and others.

We, however, consciously refrained from using these techniques. We were interested in analyzing the performance of our method without affecting the results by additional processing steps, which often introduce empirical parameters and may decrease repeatability in the comparison of the time-series scenarios. Therefore, we had to carefully select the spots for validation of the estimated flooding elevations. Our aim for developing the series of flooding extent maps was to use them for validation of integrated groundwater–surface water 3-D hydrological model. For this purpose, a similar validation method of identifying many vegetation-free spots in the entire valley had to be used to identify the presence or absence of flooding.

The inability to distinguish between river water flooding and flooding from different sources resulted in false positives and large overestimates of flooding elevations (see Fig. 6). These elevation estimates were errors only in reference to the river gauge observation, because they represented the true presence

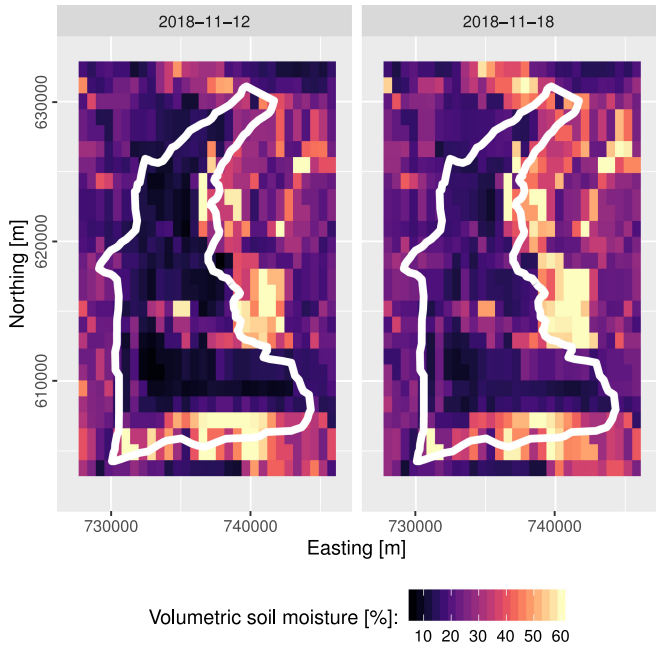

Fig. 9. Comparison of volumetric soil moisture content estimates during dry (November 12, 2018) and wet (November 18, 2018) conditions in the study area (white line) during a low-flow period. The snapshots correspond to the third and fourth panels in Fig. 7.

of patches disconnected from the river water, which originate from either groundwater discharge, precipitation, or snowmelt. To confirm this, we compared the two flood maps from dry and wet conditions in November 2018 (see Fig. 7) with SMAP/Sentinel 1 soil moisture estimates [48], which showed that together with the flooding extent increase in the remote floodplain, the soil moisture increased by approximately 10–20% (see Fig. 9). Furthermore, this was confirmed by groundwater depth data from 23 wells in the study area [49], of which 20 showed an increase of water elevation by up to 0.12 m from its initial position during the analyzed period. A similar situation was observed in North-American Prairies, where during high-soil-moisture periods, σ^0 values were lower than during low-soil-moisture periods, which indicated the presence of open water [17].

Unfortunately, we were only able to filter events occurring during the presence of snow cover (mostly wet snow and snowmelt ponding). We did not have a reference dataset to filter water patches caused by groundwater or rainwater ponding. However, these patches show the overall hydrological behavior of a study area and do not necessarily have to be filtered out of the flooding map. In other studies, the disconnected flood patches were often filtered out of the river flooding extent [8], [16], which was usually achieved using the HAND method [38]. Filtering is appropriate if a study is focused only on the analysis of flooding generated by river water and the hydrological model used is not capable to simulate the disconnected patches flooded by local groundwater discharge, rainfall, or snowmelt.

Snow cover was also responsible for the underestimation of flooding elevation and flooding extent. This was especially visible during longer periods of high snow depth, e.g., January

and February 2018 (see Fig. 7), because high snow cover depths increase radar backscatter [36]. Another explanation of this behavior could be the presence of ice, which was observed in January and February 2018 at the Burzyn cross section [33]. Ice has stronger backscatter for VV than that for VH polarization in the C-band [50], which can explain the lack of inundation detection for VV (σ^0_{VV} for ice $> t_0$) and the detection of ice cover as inundation for VH (σ^0_{VH} for ice $< t_0$).

The last identified shortcomings are a few false-negative estimations of the flood extent (see Fig. 6) in the Osowiec and Burzyn cross sections in the periods when the water elevation approaches the bankfull level. We believe that this effect was mostly related to the resolution of the Sentinel 1 data and the topography near the river channel. The microtopography of former oxbow lakes and river sediments near the channel can form a complex outflow pattern, which does not always generate a large enough water extent to be detected at Sentinel 1 resolution. This effect may be reinforced by emerging vegetation at the beginning of the growing season.

C. Advantages and Limitations of the Method

The main advantage of this method is the relatively small effort required to process a long time series of radar data. This concerns the raw (e.g., GRD) SAR data preprocessing steps that can be automatized by remote sensing software, such as SNAP. Furthermore, this concerns the method itself, which can be implemented in any scripting language capable to process spatial data, such as R or python. An advantage of this method is also its physical basis, which linearly relates the water elevation to the flooding area. The method requires, except for time series of radar data and zone delineation, only the water elevation or discharge for the corresponding days. This, however, limits the method application to catchments with at least one river gauge. Moreover, to perform a validation such as in this study, a high-quality DTM is required.

One of the most important limitations is that the method does not deal with vegetation obscuring the water and producing a patchy flooding extent. Another limitation could be the performance with SAR data from different relative orbits. In this study, we used data from only one relative orbit. Introducing more orbits would increase the time series resolution to one to three days. However, it would also introduce geometric and radiometric differences in the processed Sentinel 1 data that could decrease the quality of the estimated flooding extents.

The method was also capable of identifying water from other sources than river flooding. This was mostly due to the lack of filtering of disconnected flood patches. This can be either an advantage or disadvantage, depending on the application. If the flooding extent maps are used to calibrate or validate a hydrodynamic model, which due to its boundary condition is capable only of simulating flooding caused by river water, then any disconnected flood patches generated by floodplain water sources would be false positives. However, if an integrated hydrological model, that simulates both groundwater and surface water fluxes (as well as other hydrological processes), is used, then the flood patches originating from floodplain water would be true positives.

D. Other Approaches in the σ^0 Threshold Estimation Method

In this method, we assume that $u \propto h$, which allows us to quantify linear dependence between $U(t)$ and H using the Pearson's correlation coefficient and to omit transformation of u, e.g., using a power law. This assumption is valid in steady-state flow conditions when surface water slope is equal to the floodplain slope, and if floodplain cross section perpendicular to the river is regular, e.g., trapezoidal. When Q is used instead of H in (2), the assumption is weaker, because q is nonlinearly related to h, as illustrated, e.g., by the Manning equation [51]. Therefore, even in steady-state and regular cross section, q is nonlinearly related to u. The power law can be used to approximate the u–q relationship [18].

To account for the possible nonlinearity of u–h and u–q relationships, an additional parameter could be introduced in (2), e.g., an exponent parameter for the $U(t)$ term. The additional parameter would have to be identified simultaneously with the t_0 parameter in the correlation optimization (2). Because of that, a 2-D solver would have to be used instead of 1-D domain screening as in the proposed method. This, however, would require more computation resources. We expect that the correlation between $U(t)$ and H or Q would be higher in a 2-D than in a 1-D optimization approach. Yet, because of the characteristics of u–h and u–q relationships, which are monotonically increasing (for positive q or h), we expect that the optimum Pearson's correlation would be identified for similar t_0. This is supported by other studies that identified similar values of the t_0 threshold for Sentinel 1 data. In our study, $t_0 = -17.2$ dB for VV polarization, whereas $t_0 = -16.1$ dB was identified with use of the power transformation in [18], and $t_0 = -18.1$ dB was identified without use of the power transformation in [25].

Another approach, that would allow finding a relationship between u and h or q, could rely on the manual derivation of u by digitizing flooding extent from high-resolution visible and near-infrared (VIS–NIR) satellite imagery. In this approach, h and q could be obtained directly from river gauges, or h could be extracted indirectly from a high-resolution DEM using the water line method (described in this study). A relationship derived in this way would precisely reflect the nonlinearities related to the irregular floodplain cross section, which was not possible in our method. Yet, even this approach would not be able to account for all nonlinearities, because the time-variant surface water slope, caused by unsteady flow, would not be captured during digitization of a limited sample of the VIS–NIR satellite imagery.

V. Conclusion

In this article, we proposed a method for the estimation of the radar backscatter coefficient threshold for flood mapping. Our method automatically processed a time series of 161 SAR images with corresponding river gauge observations used as ancillary data. We showed that SAR-derived flooding extents are related to water elevations or discharges. This relation can be

used to find an optimal backscatter threshold for differentiating between flooded and nonflooded pixels using a simple search method.

The most important factor in the method was the extent of the zone in which the flooding area was calculated. Too wide zones, that include flooding from other sources than the river, decreased the correlation between flooding area and river gauge observations, which led to higher errors of flooding extent estimation. The second most important factor was the polarization used. The VH polarization led to worse flooding extent estimations than VV because of misclassification of vegetation and soil. However, the VH polarization was able to identify the ice-covered flooding extent, which was not possible for VV polarization using this method. The discharge scenarios performed worse than the water elevation scenarios because they were more nonlinearly related to flooding areas. However, the use of discharges is a reasonable alternative when water elevations are not available.

The method does not include filtering the patches in the flooding extent caused by vegetation or other objects. Therefore, the use of this method for producing data for calibration or validation of hydrodynamic models requires the identification of low vegetation spots. Otherwise, e.g., region-growing post-processing should be used. Despite the method calculating the flooding areas in a predefined zone, open water is detected in the entire image. Therefore, the flooding patches from other sources than the river are also present in the output maps. This is useful if the flooding maps are used to calibrate or validate a hydrological model that simulates processes related to the generation of these flooding patches. On the contrary, for a hydrodynamic model, which simulates the river flooding only, these flooding patches would be false positives.

Future work should be related to testing other approaches in the σ^0 threshold estimation method, which would allow us to account for nonlinearities in u–h and u–q relationships, such as power-law transformation, and assuming irregular floodplain cross sections. The method should also be tested in other areas, e.g., in urban land use or arid climate with validation based on the high-resolution VIS–NIR imagery.

ACKNOWLEDGMENT

The authors are grateful for the data provided by: European Space Agency; Polish Institute of Meteorology, and Water Management—National Research Institute; Biebrza National Park, Poland; U.S. National Ice Center.

REFERENCES

[1] N. Otsu, "A threshold selection method from gray-level histograms," *IEEE Trans. Syst., Man, Cybern.*, vol. SMC-9, no. 1, pp. 62–66, Jan. 1979.

[2] S. Long, T. E. Fatoyinbo, and F. Policelli, "Flood extent mapping for Namibia using change detection and thresholding with SAR," *Environ. Res. Lett.*, vol. 9, no. 3, Mar. 2014, Art. no. 035002.

[3] L. Smith, B. Isacks, R. Forster, A. Bloom, and I. Preuss, "Estimation of discharge from braided glacial rivers using ERS 1 synthetic aperture radar: First results," *Water Resour. Res.*, vol. 31, pp. 1325–1329, 1995.

[4] D. Sabel, V. Naeimi, F. Greifeneder, and W. Wagner, *Investigating Radar Time Series for Hydrological Characterisation in the Lower Mekong Basin*. New York, NY, USA: Springer, 2015, pp. 357–381.

[5] S. Grimaldi, Y. Li, V. Pauwels, and J. Walker, "Remote sensing-derived water extent and level to constrain hydraulic flood forecasting models: Opportunities and challenges," *Surv. Geophys.*, vol. 37, pp. 977–1034, 2016.

[6] X. Shen, E. N. Anagnostou, G. H. Allen, G. R. Brakenridge, and A. J. Kettner, "Near-real-time non-obstructed flood inundation mapping using synthetic aperture radar," *Remote Sens. Environ.*, vol. 221, pp. 302–315, 2019.

[7] D. Mason, G.-P. Schumann, J. Neal, J. Garcia-Pintado, and P. Bates, "Automatic near real-time selection of flood water levels from high resolution synthetic aperture radar images for assimilation into hydraulic models: A case study," *Remote Sens. Environ.*, vol. 124, pp. 705–716, 2012.

[8] A. Twele, W. Cao, S. Plank, and S. Martinis, "Sentinel-1-based flood mapping: A fully automated processing chain," *Int. J. Remote Sens.*, vol. 37, no. 13, pp. 2990–3004, 2016.

[9] D. Roque, N. Afonso, A. M. Fonseca, and S. Heleno, "OBIA flood delimitation assisted by threshold determination with principal component analysis," *Photogramm. Eng. Remote Sens.*, vol. 80, no. 6, pp. 551–557, 2014.

[10] V. Tsyganskaya, S. Martinis, P. Marzahn, and R. Ludwig, "Detection of temporary flooded vegetation using Sentinel-1 time series data," *Remote Sens.*, vol. 10, no. 8, 2018, Art. no. 1286.

[11] K. Uddin, M. A. Matin, and F. J. Meyer, "Operational flood mapping using multi-temporal Sentinel-1 SAR images: A case study from Bangladesh," *Remote Sens.*, vol. 11, no. 13, 2019, Art. no. 1581.

[12] L. Wan, M. Liu, F. Wang, T. Zhang, and H. J. You, "Automatic extraction of flood inundation areas from SAR images: A case study of Jilin, China during the 2017 flood disaster," *Int. J. Remote Sens.*, vol. 40, no. 13, pp. 5050–5077, 2019.

[13] C. Zhou, J. Luo, C. Yang, B. Li, and S. Wang, "Flood monitoring using multi-temporal AVHRR and RADARSAT imagery," *Photogramm. Eng. Remote Sens.*, vol. 66, no. 5, pp. 633–638, 2000.

[14] P. A. Townsend, "Mapping seasonal flooding in forested wetlands using multi-temporal Radarsat SAR," *Photogrammetric Eng. Remote Sens.*, vol. 67, no. 7, pp. 857–864, 2001.

[15] F. Frappart, F. Seyler, J.-M. Martinez, J. G. León, and A. Cazenave, "Floodplain water storage in the Negro river basin estimated from microwave remote sensing of inundation area and water levels," *Remote Sens. Environ.*, vol. 99, no. 4, pp. 387–399, 2005.

[16] M. A. Clement, C. G. Kilsby, and P. Moore, "Multi-temporal synthetic aperture radar flood mapping using change detection," *J. Flood Risk Manage.*, vol. 11, no. 2, pp. 152–168, 2018.

[17] S. Schlaffer, M. Chini, R. Pöppl, R. Hostache, and P. Matgen, "Monitoring of inundation dynamics in the North-American Prairie Pothole Region using Sentinel-1 time series," in *Proc. IEEE Int. Geosci. Remote Sens. Symp.*, 2018, pp. 6588–6591.

[18] D. Kim and W. Ahmad, "Estimation of flow in various sizes of streams using the Sentinel-1 synthetic aperture radar (SAR) data in Han River basin, Korea," *Int. J. Appl. Earth Observ. Geoinf.*, vol. 83, no. 11, 2019, Art. no. 101930.

[19] L. Pulvirenti, G. Boni, N. Pierdicca, M. Fiorini, and R. Rudari, "Combined use of multi-temporal COSMO-SkyMed data and a hydrodynamic model to monitor flood dynamics," in *Proc. IEEE Geosci. Remote Sens. Symp.*, 2014, pp. 3346–3349.

[20] S. Scarpino *et al.*, "Multitemporal SAR data and 2D hydrodynamic model flood scenario dynamics assessment," *ISPRS Int. J. Geo-Inf.*, vol. 7, no. 3, 2018, Art. no. 105.

[21] L. Jiang, H. Madsen, and P. Bauer-Gottwein, "Simultaneous calibration of multiple hydrodynamic model parameters using satellite altimetry observations of water surface elevation in the Songhua River," *Remote Sens. Environ.*, vol. 225, pp. 229–247, 2019.

[22] S. Gobeyn *et al.*, "Impact of the timing of a SAR image acquisition on the calibration of a flood inundation model," *Adv. Water Resour.*, vol. 100, pp. 126–138, 2017.

[23] L. C. Smith, B. L. Isacks, A. L. Bloom, and A. B. Murray, "Estimation of discharge from three braided rivers using synthetic aperture radar satellite imagery: Potential application to ungaged basins," *Water Resour. Res.*, vol. 32, no. 7, pp. 2021–2034, 1996.

[24] D. Kim *et al.*, "Mapping spatio-temporal water level variations over the central Congo river using PALSAR ScanSAR and Envisat altimetry data," *Int. J. Remote Sens.*, vol. 38, no. 23, pp. 702–7040, 2017.

[25] M. Wood, S. de Jong, and M. Straatsma, "Locating flood embankments using SAR time series: A proof of concept," *Int. J. Appl. Earth Observ. Geoinf.*, vol. 70, pp. 72–83, 2018.

[26] T. Berezowski, T. Bieliński, and J. Osowicki, "Floodplain inundation mapping using SAR scattering coefficient thresholding and observed discharge data," in *Proc. IEEE Int. Geosci. Remote Sens. Symp.*, Jul. 2019, pp. 4704–4707.
[27] S. Ignar *et al.*, "Temporal variability of the selected flood parameters in the Biebrza river valley," *Ann. Warsaw Univ. Life Sci.*, vol. 2, no. 43, pp. 135–142, 2011.
[28] J. Chormański *et al.*, "Flood mapping with remote sensing and hydrochemistry: A new method to distinguish the origin of flood water during floods," *Ecol. Eng.*, vol. 37, no. 9, pp. 1334–1349, 2011.
[29] F. Keizer, P. Schot, T. Okruszko, J. Chormanski, I. Kardel, and M. Wassen, "A new look at the flood pulse concept: The (ir)relevance of the moving littoral in temperate zone rivers," *Ecol. Eng.*, vol. 64, no. 0, pp. 85–99, 2014.
[30] T. Berezowski, D. Partington, J. Chormański, and O. Batelaan, "Spatiotemporal dynamics of the active perirheic zone in a natural wetland floodplain," *Water Resour. Res.*, vol. 55, no. 11, pp. 9544–9562, Nov. 2019.
[31] M. J. Wassen *et al.*, "Eco-hydrological functioning of the Biebrza wetlands: Lessons for the conservation and restoration of deteriorated wetlands," in *Wetlands: Functioning, Biodiversity Conservation, and Restoration*, vol. 191. Berlin, Germany: Springer, 2006, pp. 285–310.
[32] T. Berezowski *et al.*, "Wetlands in flux: Looking for the drivers in a central European case," *Wetlands Ecol. Manage.*, vol. 26, no. 5, pp. 849–863, 2018.
[33] PIMWM. (2020) Dane publiczne IMGW-PIB/(Public data PIMWM). (In Polish). Accessed: Feb. 25, 2020. [Online]. Available: https://dane.imgw.pl/
[34] BNP, "Digital elevation model for Biebrza national park 2015," 2015, provided upon public data request by the Biebrza national park. [Online]. Available: https://www.biebrza.org.pl/
[35] T. Berezowski, J. Chormański, and O. Batelaan, "Skill of remote sensing snow products for distributed runoff prediction," *J. Hydrol.*, vol. 524, pp. 718–732, 2015.
[36] ESA, *Report for Mission Selection: CoReH$_2$O, ESA SP-1324/(3 volume series)*. Noordwijk, The Netherlands: Eur. Space Agency, 2012.
[37] U.S. National Ice Center, "IMS daily northern hemisphere snow and ice analysis at 1 km, 4 km, and 24 km resolutions, version 1. 2014-2018 subset." 2008. Accessed: Feb. 20, 2020.
[38] C. D. Rennó *et al.*, "HAND, a new terrain descriptor using SRTM-DEM: Mapping terra-firme rainforest environments in Amazonia," *Remote Sens. Environ.*, vol. 112, no. 9, pp. 3469–3481, 2008.
[39] P. Manjusree, L. P. Kumar, C. M. Bhatt, G. S. Rao, and V. Bhanumurthy, "Optimization of threshold ranges for rapid flood inundation mapping by evaluating backscatter profiles of high incidence angle SAR images," *Int. J. Disaster Risk Sci.*, vol. 3, no. 2, pp. 113–122, 2012.
[40] L. A. K. Mertes, "Documentation and significance of the perirheic zone on inundated floodplains," *Water Resour. Res.*, vol. 33, no. 7, pp. 1749–1762, 1997.
[41] F. Henderson, "Environmental factors and the detection of open surface water areas with X-band radar imagery," *Int. J. Remote Sens.*, vol. 16, no. 13, pp. 2423–2437, 1995.
[42] B. Koetz, Z. Vekerdy, M. Menenti, and D. Fernández-Prieto, *Earth Observation for Water Resource Management in Africa*. Basel, Switzerland: MDPI AG, 2015.
[43] H. Cao, H. Zhang, C. Wang, and B. Zhang, "Operational flood detection using Sentinel-1 SAR data over large areas," *Water*, vol. 11, no. 4, 2019, Art. no. 786.
[44] S. Martinis, "Improving flood mapping in arid areas using Sentinel-1 time series data," in *Proc. IEEE Int. Geosci. Remote Sens. Symp.*, 2017, pp. 193–196.
[45] V. Tsyganskaya, S. Martinis, and P. Marzahn, "Flood monitoring in vegetated areas using multitemporal Sentinel-1 data: Impact of time series features," *Water*, vol. 11, no. 9, 2019, Art. no. 1938.
[46] D. C. Mason, I. J. Davenport, J. C. Neal, G. J. Schumann, and P. D. Bates, "A near real-time algorithm for flood detection in urban and rural areas using high resolution synthetic aperture radar images," in *Proc. 2nd Int. Conf. Space Technol.*, 2011, pp. 1–4.
[47] M. N. Sumaiya and R. S. S. Kumari, "Unsupervised change detection of flood affected areas in SAR images using Rayleigh-based Bayesian thresholding," *IET Radar, Sonar Navigat.*, vol. 12, no. 5, pp. 515–522, 2018.
[48] N. Das *et al.*, "SMAP/Sentinel-1 L2 radiometer/radar 30-second scene 3 km EASE-grid soil moisture, version 2. soil moisture dataset," 2018. Accessed: Feb. 7, 2020.
[49] BNP, "Groundwater depth dataset in Biebrza national park 1994-2019," 2020 (provided upon public data request by the Biebrza National Park). Online]. Available: https://www.biebrza.org.pl/
[50] A. M. Johansson, C. Brekke, G. Spreen, and J. A. King, "X-, C-, and L-band SAR signatures of newly formed sea ice in Arctic leads during winter and spring," *Remote Sens. Environ.*, vol. 204, pp. 162–180, 2018.
[51] D. Barr and M. Das, "Direct solutions for normal depth using the Manning equation," *Proc. Inst. Civil Eng.*, vol. 81, no. 3, pp. 315–333, 1986.

Tomasz Berezowski (Member, IEEE) was born in Warsaw, Poland, in 1986. He received the B.S. and M.S. degrees in environmental protection from the Warsaw University of Life Sciences, Warsaw, in 2010, and the Ph.D. degree in engineering from Vrije Universiteit Brussel, Brussels, Belgium, in 2015.

From 2014 to 2017, he was with the Department of Hydrology and Water Resources, Warsaw University of Life Sciences. Since 2017, he has been an Assistant Professor with the Department of Geoinformatics, Gdańsk University of Technology, Gdańsk, Poland. From 2014 to 2015, he was a Visiting Scholar at Flinders University, Adelaide, SA, Australia. He is the author of 16 JCR publications. His research interests include applications of remote sensing in hydrology, especially in hydrologic modeling.

Tomasz Bieliński was born in Jelenia Góra, Poland, in 1988. He received the Eng. and M.Eng. degrees in computer science, in 2011 and 2012, respectively, from the Gdańsk University of Technology, Gdańsk, Poland, where he is working toward the Ph.D. degree with the Department of Geoinformatics.

Since 2015, he has been a Lecturer and Research Assistant with the Gdańsk University of Technology. His main research interests include parallel processing of remote sensing data and computer systems architecture. He has experience as software developer in several scientific projects. He also worked on software for implementation of Poland and European Union law regulations.

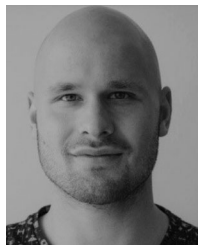

Jakub Osowicki received the B.S. degree in computer science and the M.S degree in space and satellite technologies from the Gdańsk University of Technology, Gdańsk, Poland, in 2018 and 2019, respectively.

His research interests include remote sensing, particularly in the use of polarimetric synthetic aperture radar satellite images for mapping the extent of floods.